Bulletin of the Seismological Society of America, Vol. 105, No. 6, pp. 3129–3142, December 2015, doi: 10.1785/0120150020

Ⓔ

Memory-Efficient Simulation of Frequency-Dependent Q

by Kyle B. Withers,* Kim B. Olsen, and Steven M. Day

Abstract Memory-variable methods have been widely applied to approximate frequency-independent quality factor Q in numerical simulation of wave propagation. The frequency-independent model is often appropriate for frequencies up to about 1 Hz but at higher frequencies is inconsistent with some regional studies of seismic attenuation. We apply the memory-variable approach to frequency-dependent Q models that are constant below, and follow a power-law above, a chosen transition frequency. We present numerical results for the corresponding memory-variable relaxation times and weights, obtained by nonnegative least-squares fitting of the $Q(f)$ function, for a range of exponent values; these times and weights can be scaled to an arbitrary transition frequency and a power-law prefactor, respectively. The resulting memory-variable formulation can be used with numerical wave-propagation solvers based on methods such as finite differences (FDs) or spectral elements and may be implemented in either conventional or coarse-grained form. In the coarse-grained approach, we fit effective Q for low-Q values (<200) using a nonlinear inversion technique and use an interpolation formula to find the corresponding weighting coefficients for arbitrary Q. A 3D staggered-grid FD implementation closely approximates the frequency–wavenumber solution to both a half-space and a layered model with a shallow dislocation source for Q as low as 20 over a bandwidth of two decades. We compare the effects of different power-law exponents using a finite-fault source model of the 2008 M_w 5.4 Chino Hills, California, earthquake and find that $Q(f)$ models generally better fit the strong-motion data than the constant Q models for frequencies above 1 Hz.

Online Material: Figures comparing finite difference and frequency–wavenumber seismograms for an elastic layered-model point source simulation. Median spectral acceleration centered at 1 s and Fourier amplitude centered at 0.25 and 2.25 Hz for strong ground motion recordings and synthetics from the Chino Hills earthquake.

Introduction

Anelastic attenuation, modeled by the quality factor Q, is needed for accurate simulation of seismic-wave propagation, which plays an important role in many areas of seismology, including strong ground motion prediction (e.g., Olsen *et al.*, 2000; Komatitsch *et al.*, 2004; Cui *et al.*, 2010; Graves and Aagaard, 2011), seismic imaging (e.g., Savage *et al.*, 2010; Tape *et al.*, 2010; Lee and Chen, 2014), and forensic seismology (e.g., Xie, 2005). Simulation of attenuation using time-domain techniques is not computationally feasible when the viscoelastic stress–strain relationship is expressed in convolutional form. The problem has been made tractable by approximating the stress–strain relationship with a discrete decay spectrum, which gives rise to what is known as memory variables in the simulation, in which each memory variable represents a relaxation process, with a characteristic time constant, satisfying a first-order differential equation (Day and Minster, 1984; Emmerich and Korn, 1987; Blanch *et al.*, 1995). The relaxation time constants can be chosen, and the memory variables weighted, such that, collectively, the relaxations approximate a target $Q(f)$ spectrum and the associated dispersion. The number of relaxation times is usually chosen so that the superposition of the memory variables accurately models Q across the desired bandwidth.

In principle, all relaxation times operate on each stress component for each volume element in the simulation, and the memory-variables approach has often been implemented in that form. The added storage and calculations for an anelastic simulation are directly proportional to the number of relaxation times introduced into the approximation; in very large simulations, especially in 3D, the added storage and computations may become burdensome. To decrease the computational burden,

*Also at University of California, San Diego, Institute of Geophysics and Planetary Physics, 9500 Gilman Drive, La Jolla, California 92093.

Day (1998) introduced the coarse-grained approach for a 3D anelastic medium, in which the relaxation times and weights are distributed across the unit cells, approximating the intrinsic attenuation with a coarser sampling. Day and Bradley (2001) implemented the coarse-grained approach in a staggered-grid finite-difference (FD) method, and the FD implementation was adapted to very low-Q media by Graves and Day (2003) and to discontinuous media by Kristek and Moczo (2003). The coarse-grained approach has also been adapted to the finite-element method by Ma and Liu (2006) and to the spectral element method by van Driel and Nissen-Meyer (2014).

In previous studies, numerical simulations have mainly been restricted to constant (frequency-independent) Q models, in which the memory-variable weights have been chosen with various algorithms (e.g., Emmerich and Korn, 1987, and Xu and McMechan, 1998, although these approaches allowed for a more general Q) or simply set equal to a constant (Day and Bradley, 2001). Recently, Fitchner and van Driel (2014) modeled Q with a power-law dependence on frequency across the entire model bandwidth. These approaches have been mostly used for simulations confined to frequency $f \leq$ 1–2 Hz (e.g., Olsen *et al.*, 2000; Komatitsch *et al.*, 2004; Cui *et al.*, 2010). With the recent addition of source complexities (such as surface roughness) to simulations of earthquake sources, ground motion can now be simulated by dynamically consistent sources, retaining frequencies up to ∼10 Hz. Such simulations are generally consistent with the spectral characteristics of recorded data (Dunham *et al.*, 2011; Shi and Day, 2013). With the continued advancement of high-performance computing, high-frequency ground-motion prediction can be extended to significant distances from the fault using highly scalable numerical techniques.

In the frequency range below about 1 Hz, observations show that a frequency-independent Q relationship is often an appropriate approximation (e.g., Liu *et al.*, 1976). At higher frequencies, however, seismic observations frequently are more consistent with models in which Q is an increasing function of frequency (e.g., Raoof *et al.*, 1999; Lekic *et al.*, 2009; McNamara *et al.*, 2012; Phillips *et al.*, 2013). This behavior is typically found to follow the form of a power law:

$$Q(f) = Q_0 \times (f/f_0)^{\gamma}, \tag{1}$$

in which f_0 is a reference frequency with Q_0 and γ constants that vary with the region and geology. For example, Erickson *et al.* (2004) found Q_0 to be in the 100–150 range and $\gamma =$ 0.6–0.7 for California but found Q_0 to be around 650 and $\gamma =$ 0.3–0.4 in the eastern United States, showing a weaker frequency dependence for *Lg* shear waves. Additionally, Phillips *et al.* (2013) found evidence that the frequency dependence is stronger (larger γ) in low-Q tectonic regions compared with high-Q stable areas.

Here, we use both linear and nonlinear least squares to find the weights that scale the memory variables to fit a target Q model, with no frequency dependence up to a transition frequency f_T and following a power-law formulation above this transition:

$$Q(f) = \begin{cases} Q_0 & 0 < f < f_T \\ Q_0 \times (f/f_T)^{\gamma} & f > f_T \end{cases}, \tag{2}$$

in which Q is the quality factor, Q_0 is the low-frequency value of Q, and $0 \leq \gamma \leq 1$. We solve for a range of possible values of γ (0.0–0.9), linearizing the relationship between $1/Q$ and memory-variable weights for high Q (>200) through a low-loss approximation and fitting the effective Q or harmonic average over the coarse-grained cell for low-Q values (15–200). Our technique begins with a specified set of relaxation times appropriate to the bandwidth of the simulation and then fits the corresponding memory-variable weights to the model of equation (2). We use a nominal value Q_0^* for Q_0 for high Q, so that the resulting set of weights can then be scaled to give the target Q_0 by multiplying them by the factor Q_0^*/Q_0. For low Q, we fit a discretized range of Q values and solve for a simple formula so that the weights can be quadratically interpolated. This procedure yields a $Q(f)$ function that matches equation (2), typically within 4% across the spectrum 0.1–10 Hz and becoming slightly more inaccurate for high-exponent power-law models ($\gamma > 0.7$) near the transition frequency at low Q.

The method is implemented into a fourth-order staggered-grid FD code using the coarse-grained technique with eight relaxation times distributed with periodicity of two nodes (as in Day, 1998), with a single relaxation time at each node. To verify the method, we compare synthetic seismograms computed with the FD program to those from a frequency–wavenumber (f-k) code, and we illustrate the importance of including $Q(f)$ in ground-motion estimation by simulating the 2008 M_w 5.4 Chino Hills, California, earthquake.

Background

This section reviews the previous development of the conventional memory-variable method, used as a starting point for our technique. The result is an (approximate) expression for Q in terms of N weighting coefficients and N relaxation times.

Anelastic attenuation is implemented into time-stepping routines through the use of memory variables, whereby energy is dissipated from the system. The isotropic stress (σ)–strain (ϵ) relation can be written as a set of relations of the form

$$\sigma(t) = M_u[\epsilon(t) - \Sigma_{k=1}^{N} \xi_k(t)], \tag{3}$$

in which M_u is the unrelaxed modulus and ξ_k is a memory variable. Equation (3) represents either mean stress in terms of volumetric strain (with M_u representing a bulk modulus) or a deviatoric stress component in terms of the corresponding deviatoric strain component (with M_u representing the shear modulus). The memory variables ξ_k follow the N first-order differential equations (Day, 1998):

$$\tau_k \frac{d\xi_k(t)}{dt} + \xi_k(t) = \lambda_k \epsilon(t), \tag{4}$$

at each relaxation time τ_k with weight λ_k; our definition of λ_k is equivalent to the product $(\delta M/M_u)\lambda_k$ of Day (1998, their

equation 14), in which δM is the modulus defect (i.e., the unrelaxed modulus minus the relaxed modulus). These may be time stepped using standard approximations (e.g., Day, 1998):

$$\xi_k(t+\delta t) = e^{-\delta t/\tau_k}\xi_k(t-\delta t) + \lambda_k(1-e^{-\delta t/\tau_k})\epsilon(t). \quad (5)$$

The result of approximating the stress–strain relation in the form of equation (3) is that the complex viscoelastic modulus (as a function of angular frequency ω) takes the form

$$M(\omega) = M_{\mathrm{u}}\left(1 - \Sigma_{k=1}^{N}\frac{\lambda_k}{1+i\omega\tau_k}\right). \quad (6)$$

One definition of Q is

$$Q^{-1}(\omega) = \frac{Im[M(\omega)]}{Re[M(\omega)]} = \frac{\Sigma_{k=1}^{N}\frac{\lambda_k\omega\tau_k}{1+(\omega\tau_k)^2}}{1-\Sigma_{k=1}^{N}\frac{\lambda_k}{1+(\omega\tau_k)^2}}; \quad (7)$$

and, if we assume the low-loss approximation $\delta M \ll M_{\mathrm{u}}$, this becomes

$$Q^{-1}(\omega) = \Sigma_{k=1}^{N}\frac{\lambda_k\omega\tau_k}{1+(\omega\tau_k)^2}, \quad (8)$$

which gives a good approximation for $Q \geq 20$ in the memory-intensive non-coarse-grained approach. In the case in which the memory-efficient coarse-grained technique is used, Graves and Day (2003) determined the harmonic average of the modulus is more accurate than equation (6) for $Q < 20$. In addition to representing Q for a discrete approximation to an anelastic model with continuous relaxation spectrum (Day and Minster, 1984), equation (7) can also be interpreted as the Q of a spring-dashpot network model of either the generalized Maxwell or generalized Zener type (e.g., Moczo, 2005). It takes the form of a sum of Debye peaks centered at frequencies given by the inverses of the respective relaxation times.

Wavespeeds input to numerical simulations usually correspond to measured or hypothesized wavespeeds at some finite reference frequency. The reference frequency has to be taken into account in the computation of the unrelaxed elastic moduli from the input wavespeeds. With a given choice of relaxation times and weighting coefficients, the unrelaxed modulus can be expressed in terms of the phase velocity c at reference frequency ω_0 by

$$M_{\mathrm{u}} = \frac{c^2\rho\left(Re\left[\sqrt{\frac{1}{1+iQ^{-1}(\omega_0)}}\right]\right)^{-2}}{Re\left[1-\Sigma_{k=1}^{N}\frac{\lambda_k}{1+iw_0\tau_k}\right]}, \quad (9)$$

in which

$$c(\omega_0) = \sqrt{\frac{Re[M(\omega_0)]}{\rho}}\left(Re\left[\sqrt{\frac{1}{1+iQ^{-1}(\omega_0)}}\right]\right)^{-1}. \quad (10)$$

Here, ρ is density, and M is given by equation (6) and Q by equation (7). In the case of effective Q, the modulus is found from

$$M_E(\omega) = N \times \left(\Sigma_{k=1}^{N}\frac{1}{M_k(\omega)}\right)^{-1}, \quad (11)$$

in which

$$M_k(\omega) = M_u\left(1-\frac{\lambda_k}{1+i\omega\tau_k}\right) \quad (12)$$

and Q in equations (9) and (10) is replaced by

$$Q_E^{-1}(\omega) = \frac{Im[M_E(\omega)]}{Re[M_E(\omega)]}. \quad (13)$$

Assuming material homogeneity across the coarse-grained cell, equation (9) then becomes

$$M_{\mathrm{u}} = \frac{c^2\rho\left\{Re\left[\sqrt{\frac{1}{1+iQ^{-1}(\omega_0)}}\right]\right\}^{-2}}{N \times Re\left\{\left[\Sigma_{k=1}^{N}\left(1-\frac{\lambda_k}{1+iw_0\tau_k}\right)^{-1}\right]^{-1}\right\}}. \quad (14)$$

With these expressions, velocity dispersion corresponding to the defined Q function is accurately accounted for.

Method

It remains to describe the method for selecting the relaxation times and weights to approximate $Q(f)$; in previous applications, the target has typically been a frequency-independent Q function. When the τ_k are approximately logarithmically spaced, the frequency-independent Q model is well fit with nearly equal λ_k for each relaxation time (e.g., Day, 1998, found that even exactly equal-value λ_k gave a good fit, within 5% tolerance, to frequency-independent Q).

In this article, we generalize the above approach to include power-law $Q(f)$. This generalization is done by numerical fitting of λ_k to the target $Q(f)$ (equation 2). Here, we set τ_k to be equally distributed logarithmically:

$$\ln\tau_k = \ln\tau_{\mathrm{m}} + \frac{2k-1}{16}(\ln\tau_{\mathrm{M}} - \ln\tau_{\mathrm{m}}), \quad (15)$$

in which τ_{m} corresponds to the minimum relaxation time and τ_{M} the maximum, the lower, and upper absorption-band cutoffs.

The best fits are typically obtained when these limits are set outside the bandwidth of computational interest. For large Q, we use constrained least squares to solve for λ_k in equation (8) to fit a target Q function of the form in equation (2) by minimizing the sum of the squares. The λ_k are constrained to be positive in the inversion to ensure that energy is dissipated from the system. Because equation (8) is linear in λ_k, solving for λ_k for one value of Q_0 (denoted Q_0^*) allows the weights to be scaled to any other value of Q_0, giving the same target shape as a function of frequency. For simplicity, we set $Q_0^* = 1$ (and the fitted weights subsequently can be scaled to arbitrary Q_0 by multiplication by $1/Q_0$). The low-loss approximation used here closely

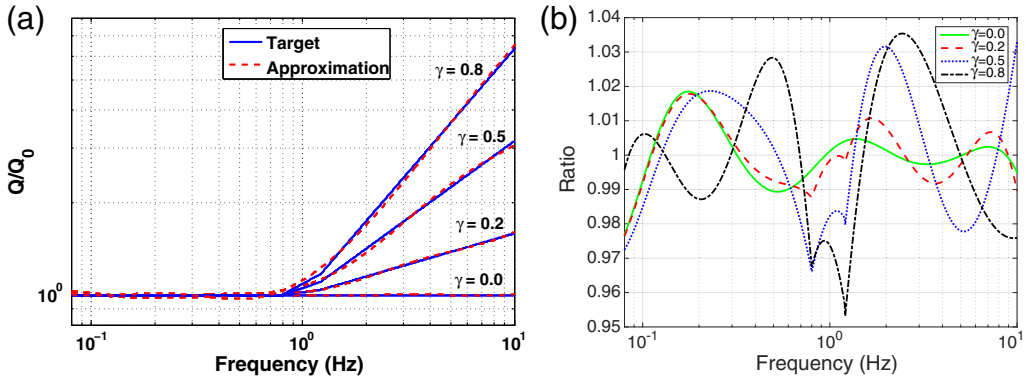

Figure 1. (a) Comparison of fits obtained between model Q (dashed line) and target Q (solid line) for several values of γ in equation (2) using the low-loss approximation as in equation (8) for an unscaled Q. (b) Ratio between target model and approximations shown in (a). The color version of this figure is available only in the electronic edition.

approximates Q (in the form of equation 7) for $Q_0 > 50$. As Graves and Day (2003) pointed out, once scaled to the desired Q_0, the sum of the weights must be bounded above by 1 to ensure stability (and the sum is bounded below by 0, because each weight is nonnegative). This condition is satisfied for all λ_k after scaling for $Q_0 > 50$ for the range of γ solved for here. The $Q(f)$ model generated by this technique can also be shifted in frequency, so the transition to a power-law model occurs at any specified frequency f_T. This frequency shift is achieved by dividing the relaxation times by the desired factor; the weights remain unchanged.

Graves and Day (2003) analyzed the coarse-grained low-Q accuracy and determined the best results are obtained when using the harmonic average of the moduli over the volume of the coarse-grained cell to determine the coefficients. We use a nonlinear least-squares approach to fit equation (11) based on the conjugate gradient method with the effective weights bounded between 0 and 1 and solve for the weighting coefficients for each integer value of Q ranging from 15 to 220. We then inverted for the coefficients (using least squares) a_k and b_k in the expression

$$\lambda_k = \frac{a_k}{Q^2} + \frac{b_k}{Q} \tag{16}$$

that fits Q accurately to within 5% (and generally much better) between 0.1 and 10 Hz. This is similar in concept to the interpolation technique proposed by Liu and Archuleta (2006) but uses a simpler formula with fewer coefficients. We chose this approach up to $Q < 200$ after performing plane-wave tests and determining that even large values of Q (>50) can be inaccurately modeled using the arithmetic modulus for wide bandwidths (more than two decades) in the coarse-grained approach, particularly when the weighting coefficients vary significantly in magnitude.

Figure 1a shows an example of the fits between the target Q spectrum and the approximation for various power-law exponents with $N = 8$ in equation (8), using the linear technique (applicable for large Q). The weights scale the individual terms (Debye peaks) in the summation of equation (8), and these terms superpose to give an approximation to the target spectrum. Here, we have chosen the transition frequency f_T to be 1 Hz and implemented a transition region between 0.8 and 1.2 Hz, in which the Q spectrum is defined as a power-law function with $\gamma/2$. This region allows a better fit when using least squares to invert for the weights, because a sharp transition is impossible to fit using the superposition of Debye peaks. Figure 1b plots the ratio between the target spectrum and the approximation for the same power-law exponents used in Figure 1a. It is clear that the fits are within a 5% tolerance across the entire bandwidth. The ratio is oscillatory about 1 (a perfect fit) due to the overlap of the Debye peaks.

Table 1 lists the minimum and maximum relaxation times used for each power-law exponent and the corresponding weights. We limited this table to positive values and to the range $\gamma = 0.0$–0.9, because γ can never be > 1 (Q^{-1} can never fall off faster than ω due to the shape of the Debye peak). Our technique is entirely general, in the sense that the weights determined in this manner can be used in either a conventional memory-variable implementation (i.e., in which the memory variables associated with all N relaxation times are calculated and summed, as in equation 3, at every stress node) or a coarse-grained implementation. In the latter case, there is an additional scale factor N related to the increased volume element represented by each memory variable in the coarse-grained discretization: λ_k on the right side of equation (4) is replaced by w_k, in which $w_k = N\lambda_k$ (Day, 1998, equation 43), for $N = 2^3$ for a 3D FD medium with a periodicity factor of 2. Note that some coefficients are near zero, indicating there is little contribution from that relaxation time; this indicates the bandwidth could be chosen to be wider and most likely still obtain accurate fits.

We found the given choice of relaxation times performs well for the technique for low Q, in which example spectra and fits are plotted in Figure 2 for $Q = 20$ using the interpolation formula as in equation (16) and the coefficients in Table 2. Here, w_k already implicitly includes the factor N in λ_k, so no normalization is required. It is evident that toward the low end

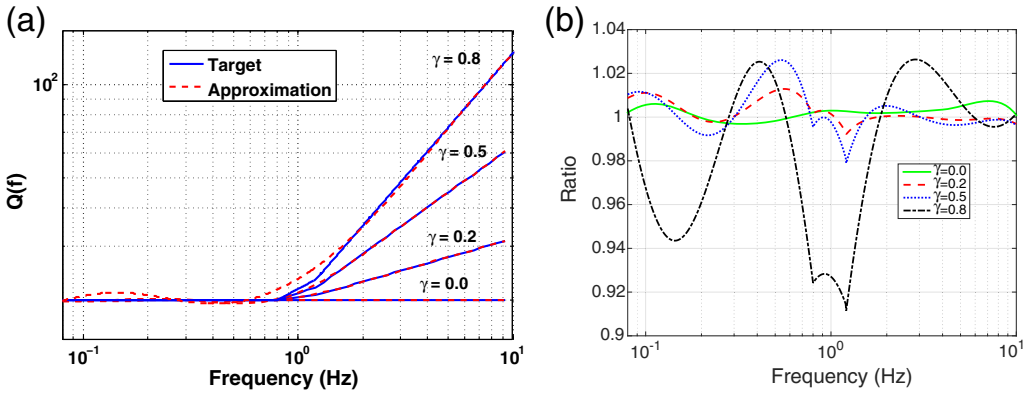

Figure 2. (a) Comparison of fits obtained between model Q (dashed line) and target Q (solid line) for several values of γ in equation (2) using the interpolation coefficients in equation (15) for effective Q in equation (12) at an example value of $Q = 20$. (b) Ratio between target model and approximations shown in (a). The color version of this figure is available only in the electronic edition.

of our Q range, it becomes harder for high power-law exponents to fit the transition region within 5%. Inverting for the weighting coefficients and relaxation times simultaneously would allow for a denser distribution of relaxation times near sharp changes or complex regions in the Q spectrum. However, more accurate fits in the frequency domain do not necessarily transmit to the actual coarse-grained time domain simulations, due to the dependence on the relative magnitude between coefficients and the choice of bandwidth. In practice, this misfit is probably negligible when comparing synthetics with real data, as the resolution of Q is significantly lower than this.

To accommodate both shear and bulk losses, it is convenient to absorb the unrelaxed moduli into the forcing term for the memory-variable evolution equation (4) (so the memory variables have the same dimensions as stress) and to remove the modulus factor on the memory variables in stress–strain equation (3). Then, adding the respective evolution equations for shear and bulk, we obtain

$$\tau_k \frac{d\xi_{ij}}{dt} + \xi_{ij} = \lambda_k \left\{ 2\mu_u Q_{s0}^{-1} \epsilon_{ij} + \left[\left(\kappa_u + \frac{4}{3}\mu_u \right) Q_{p0}^{-1} - 2\mu_u Q_{s0}^{-1} \right] \epsilon_{kk}\delta_{ij} \right\} \tag{17}$$

(following Day and Bradley, 2001), in which ϵ_{ij}, ϵ_{kk}, μ_u, and κ_u are the deviatoric and volumetric strains and the unrelaxed shear and bulk moduli, respectively. Q_{s0}^{-1}, Q_{p0}^{-1} are reference values of Q_s^{-1}, Q_p^{-1}, which differs from Day and Bradley (2001), because $\delta M/M_u$ has now been absorbed into the weights. Adding the bulk and shear equations for stress, equation (3) becomes

$$\sigma_{ij} = 2\mu_u \epsilon_{ij} + \left(\kappa - \frac{2}{3}\mu_u \right) \epsilon_{kk}\delta_{ij} - \Sigma_{l=1}^{N} \xi_{ijl}. \tag{18}$$

The time-differentiated form of equation (17) gives a first-order ordinary differential equation that one can solve for the memory variable $\dot{\xi}_{ij}$, given the strain rate $\dot{\epsilon}_{ij}$. The stress rate $\dot{\sigma}_{ij}$ can then be calculated from $\dot{\xi}_{ij}$ and $\dot{\epsilon}_{ij}$. For a fixed set of weights, the right side of equation (17) scales linearly with Q_0^{-1}, as noted earlier (assuming $Q \gg 1$).

We implemented our technique using the memory-efficient coarse-grained approach of Day and Bradley (2001) described earlier, using a scalable staggered-grid velocity-stress FD method that is fourth-order accurate in space and second-order accurate in time (Cui *et al.*, 2010). The weights are distributed with a period of two nodes, in the same periodic scheme as the corresponding relaxation times. Here, the memory variables ξ_{ij} are collocated with the stresses σ_{ij} and the summation in equation (18) is removed, becoming

$$\sigma_{ij} = 2\mu_u \epsilon_{ij} + \left(\kappa - \frac{2}{3}\mu_u \right) \epsilon_{kk}\delta_{ij} - \xi_{ij}, \tag{19}$$

and λ_k in equation (17) replaced by w_k. The implementation assumes that Q_κ and Q_μ (in which κ and μ correspond to the bulk and shear modulus, respectively) have identical frequency dependence, though they may have different prefactors Q_0. For $Q > 200$, this simplification allows us to use the same set of weights for both bulk and shear attenuation (scaled to their respective Q_0 values), though this simplification is not necessary in our approach. For $Q < 200$, or when using independent shear and bulk Q spectra, two different sets of weights are used for the bulk and shear components.

Numerical Tests

We performed several simulations using simple earth models with a shallow dislocation source. To verify our technique, we modified an f-k code (Zhu and Rivera, 2002) to account for the dispersion associated with a power-law $Q(f)$ and used the frequency-dependent modulus as given by equation (6) for the given choice of relaxation times and weights to find the complex wavenumber used in the computation. We used an iterative approach to solve for $Q^{-1}(\omega)$ as given by equation (7), in which first the weights are set to some initial value (zeros work fine) and inserted into the term

Table 1
Relaxation Times and Weight Coefficients for a Range of Power-Law Exponents

γ	0.0	0.1	0.2	0.3	0.4	0.5	0.6	0.7	0.8	0.9
τ_m	0.0032	0.0032	0.0032	0.0032	0.0032	0.0032	0.0032	0.0066	0.0066	0.0085
τ_M	15.9155	15.9155	15.9155	15.9155	15.9155	15.9155	15.9155	3.9789	3.9789	3.9789
w_1	0.8867	0.3273	0.001	0.001	0.001	0.2073	0.3112	0.1219	0.0462	0.001
w_2	0.8323	0.8478	0.804	0.6143	0.4639	0.1872	0.001	0.001	0.001	0.001
w_3	0.5615	0.369	0.2005	0.0918	0.001	0.001	0.001	0.001	0.001	0.001
w_4	0.811	0.9393	1.0407	1.1003	1.1275	1.081	1.0117	0.2999	0.1585	0.1935
w_5	0.4641	0.4474	0.4452	0.4659	0.509	0.6016	0.7123	1.3635	1.4986	1.5297
w_6	1.044	1.0434	1.0349	1.0135	0.9782	0.912	0.8339	0.001	0.001	0.001
w_7	0.0423	0.044	0.0497	0.0621	0.082	0.1186	0.1616	0.5084	0.4157	0.1342
w_8	1.7275	1.7268	1.7245	1.7198	1.7122	1.6984	1.6821	1.2197	1.3005	1.5755

Power laws using γ as in equation (2) with $Q_0 = 1$. These weights can scale to any $Q > 20$ with accuracy within 5%. The minimum relaxation time τ_m was adjusted for higher values of γ to optimize the fits. Here, $w_k = N\lambda_k$, in which $N = 8$.

Table 2
Relaxation Times and Interpolation Coefficients for a Range of Power-Law Exponents

γ	0.0	0.1	0.2	0.3	0.4	0.5	0.6	0.7	0.8	0.9
a_1	−27.5	7.37	31.8	43.7	41.6	20.0	8.08	1.99	5.16	−0.811
a_2	−34.1	−37.6	−42.0	−43.4	−41.1	−23.07	−13.0	−2.7	−8.2	0
a_3	−1.62	13.1	25.7	34.3	38.0	31.4	25.4	0	0	0
a_4	−27.7	−36.1	−40.8	−41.4	−43.2	−25.1	−10.4	41.3	58.9	56.03
a_5	14.6	12.3	7.02	−2.87	5.63	−45.2	−75.9	−88.8	−108.6	−116.9
a_6	−52.2	−51.4	−49.2	−45.3	−73.0	−27.8	−13.2	0	15.02	22.0
a_7	72.0	69.0	65.4	60.9	103.0	45.9	35.7	40.7	−5.88	0.03
a_8	−82.8	−83.1	−83.2	−83.1	−164.	−81.6	−79.9	−76.6	−46.5	−61.9
b_1	7.41	4.165	1.612	−0.1091	−0.734	−0.435	−0.196	0.418	0.212	0.162
b_2	6.02	5.52	5.08	4.58	3.82	2.67	1.81	0.59	0.345	0
b_3	4.68	3.47	2.28	1.19	0.393	−0.0434	−0.394	0	0	0
b_4	6.28	7.210	7.931	8.39	8.67	8.245	7.657	2.18	0.813	0.797
b_5	3.88	3.61	3.46	3.53	3.32	4.847	6.17	11.0	12.4	13.02
b_6	8.17	8.193	8.15	8.02	8.58	7.19	6.36	0	−0.283	−0.402
b_7	0.529	0.498	0.511	0.592	−0.419	1.15	1.68	1.95	1.42	−0.0006
b_8	13.19	13.13	13.07	13.0	14.9	12.8	12.7	11.3	11.7	12.5

in the denominator of equation (7). The resulting expression (identical to the low-loss approximation of equation 8 divided by a factor) is fit by using linear least squares. These weighting coefficients are used in the next iteration, and the procedure is continued in succession until there is negligible change in the coefficients or $Q(\omega)$ is fit to within a certain tolerance (2%–3% is typically as accurate as can be achieved for fixed τ_k).

We use a double-couple buried point source equivalent to right-lateral slip with strike 90°, dip 90°, and rake 0° at a depth of 1.8 km, using the cosine–bell moment-rate function:

$$\dot{M}(t) = \begin{cases} M_0(1 - \cos(2\pi t/T) & 0 < t < T \\ 0 & \text{otherwise} \end{cases}, \qquad (20)$$

with $T = 0.2$ s and $M_0 = 10^{16}$ N·m, equating to an M_w 4.6 earthquake. We use a grid spacing of 40 m and a time step of 0.002 s. The upper-frequency limit (i.e., the frequency up to which the solution is accurate to within a specific tolerance) scales with minimum wavespeed V_S. For example, for a minimum V_S of 2000 m/s and a resolution criterion of five grid points per minimum shear wavelength, the upper limit of this grid is 10 Hz. We constructed our model domain to be large enough to have no reflections from boundaries at the receiver station during the simulated time. The source is averaged across two depth points in the FD program, because the shear stress σ_{xy} in our scheme is located one-half grid point below the target grid location. Because the horizontal components of the staggered grid are located one-half point below the free surface, we also averaged the horizontal components of the receiver stations to be closer to the target geometry (Gottschämmer and Olsen, 2001).

First, we compare the computed time histories obtained with a purely elastic (infinite Q) model to determine the accuracy of the FD solution for the prescribed model parameters. Here, we set $V_P = 6000$ m/s, $V_S = 3464$ m/s, and $\rho = 2700$ kg/m^3. Figure 3 shows seismograms and the Fourier spectra for each component of a surface station located at a horizontal distance of 15 km from the source with an azimuth of 53.13° from north. The seismograms have been bandpassed between 0.2 and 10 Hz using a fourth-order,

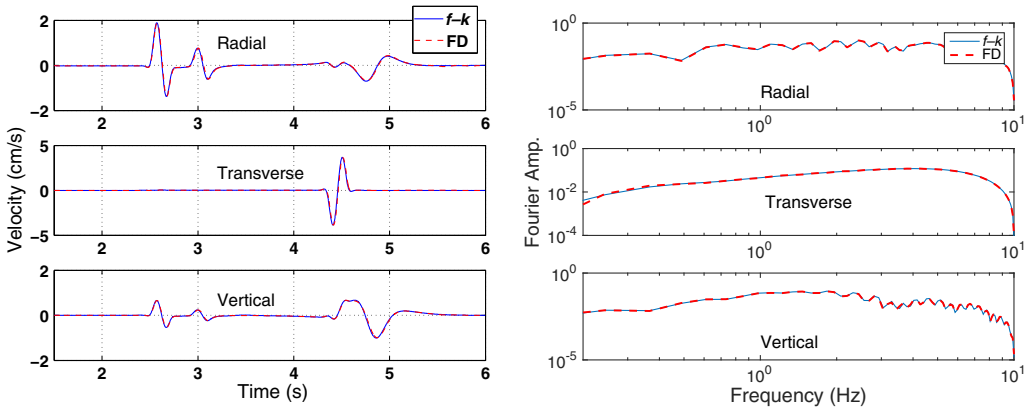

Figure 3. Half-space point-source test: comparison of frequency–wavenumber (f-k) and finite-difference (FD) results for an elastic medium. The color version of this figure is available only in the electronic edition.

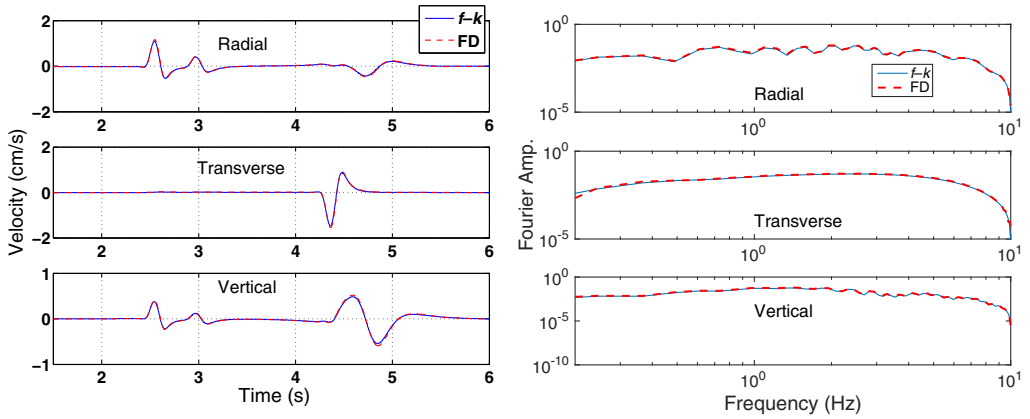

Figure 4. Half-space point-source test: comparison of f-k and FD results for a constant Q model with $\gamma = 0.0$. The color version of this figure is available only in the electronic edition.

zero-phase Butterworth filter; a reference frequency of $f_0 = 1$ Hz was used for calculating the unrelaxed modulus. We used the time–frequency representations of misfit between two seismograms, classified as envelope misfit (EM) and phase misfit (PM) as in Kristekova *et al.* (2009), to quantitatively determine the match and found arrival times of all major phases are reproduced with phase error $< 1\%$ and peak amplitudes are matched with relative error less than 2%. Fourier spectral amplitudes are nearly identical in the two solutions. The Rayleigh wave (4.5–5.5 s, radial and vertical components) is free of visible spurious oscillations and reproduces the wavenumber-integration solution with considerable precision.

Next, we use a viscoelastic half-space model simulating constant Q (i.e., a power-law exponent of 0.0, using the values listed in Table 2), in which we set $Q_{s0} = Q_{p0} = 50$. Figure 4 plots the results for the same surface station as located in Figure 3; it is evident that the two solutions are very similar and that the FD synthetics match the analytical counterparts to high accuracy, demonstrating the method is working well, even in the presence of the free surface. EM and PM here are less than 6% and 2%, respectively, for all components. By optimizing the weighting coefficients for effective Q, we are able to obtain better accuracy here than simply setting the coefficients equal to one another, as in Day and Bradley (2001).

Next, we implement our routine in a half-space using a power-law model with an exponent of 0.6, again with low-frequency $Q_{s0} = Q_{p0} = 50$, with Q increasing above the reference frequency of 1 Hz in the form of equation (2) using the coefficients in Table 2. The results are shown in Figure 5 for the same surface station as in Figures 3 and 4. It is evident in the seismograms that less energy has been attenuated and that the Fourier spectra have more energy at frequencies > 1 Hz, compared with the constant-Q model. The close fit between the f-k and FD waveforms indicates that our technique works well for all phases present in the uniform half-space, with even better accuracy than in the constant Q model, in which maximum EM and PM here are less than 2% and 1%, respectively.

To further verify our technique, we used a simple layered model (see Table 3) composed of a thin velocity layer

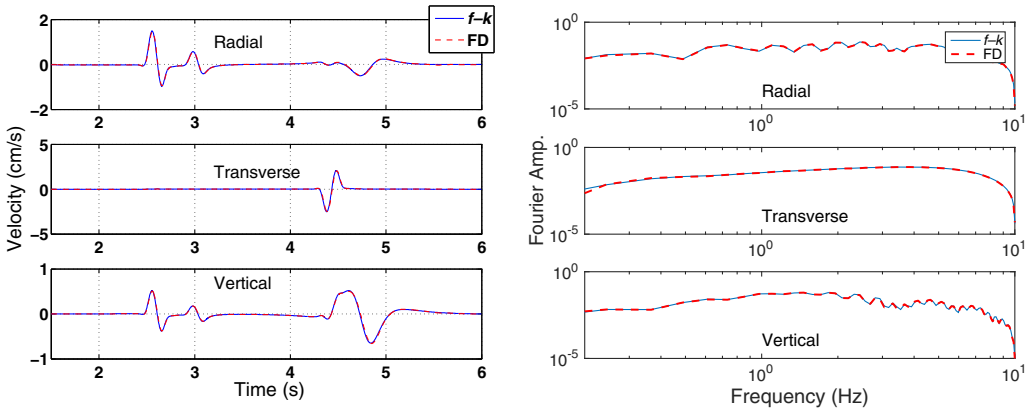

Figure 5. Half-space point-source test: comparison of f-k and FD results for a $Q(f)$ model in which $\gamma = 0.6$. The color version of this figure is available only in the electronic edition.

over a half-space, using a power-law model, $\gamma = 0.6$, with Q_{s0} and Q_{p0} values of 20 in the low-velocity layer and 210 in the underlying half-space. This problem tests the method in the presence of strata of large contrasting Q, as well as seismic velocity, and also tests its performance for Love waves.

Figure 6 shows the comparison between the f-k and FD results. It is clear that the two techniques compare very well with one another, even with Q as low as 20 and a sharp Q contrast. EM and PM here are within 5% and 2%, respectively, for the first 5 s, but they increase to 8%–10% for EM and 2% for PM for the later surface-wave arrivals. The corresponding goodness-of-fit values are above 9 in the scale used in Kristekova *et al.* (2009), which is classified as an excellent fit. For reference, the elastic case is plotted in Ⓔ Figure S1 (available in the electronic supplement to this article), with maximum EM of 3% and PM of 1%. The harmonically averaged Q over the coarse-grained cell in the shallow layer and arithmetically averaged Q in the underlying half-space is seen to work well even in the presence of layer discontinuities. The larger misfits in the later arrivals would likely be smaller if heterogenous Q across the coarse-grain cell were implemented, allowing a sharper transition in Q, but we find that we have sufficient accuracy here for a much higher contrast in Q than would likely be present within the real earth. For frequency-independent Q, Kristek and Moczo (2003) show the coarse-grained scheme loses accuracy in the presence of sharp discontinuities involving very low Q, and they propose an alternative coarse-grained formulation that is more accurate in that limit. Those results for discontinuous models are likely to apply also to the power-law case when $Q_0 \ll 20$.

Table 3
Media Parameters Defined in Layered Model

V_P (m/s)	V_S (m/s)	Density (kg/m^3)	Q_{P0}	Q_{S0}	γ	Thickness (m)
5196	3000	2550	20	20	0.6	1000
6000	3464	2700	210	210	0.6	–

Applications

We have shown that we obtain accurate seismograms using a frequency-dependent Q model and that there are differences in both the amplitude and frequency content compared with a constant-Q model. To demonstrate the importance of $Q(f)$, here we model ground motion for the 2008 M_w 5.4 Chino Hills, California, earthquake and compare results for different power-law Q models against strong-motion data. We use a finite-fault source model adapted from Shao *et al.* (2012), obtained by inversion of local earthquake records, to model the event. Even though their model was only constrained by data up to 2.5 Hz, there is significant energy in their source above this threshold (as shown by Taborda and Bielak, 2014), so we design our simulation to numerically resolve frequencies up to 4 Hz with 6.25 points per minimum wavelength. We use the Southern California Earthquake Center (SCEC) Community Velocity Model v.4 (Magistrale *et al.*, 2000; Kohler *et al.*, 2003), limiting the minimum shear-wave velocity to 200 m/s, and set the P-wave velocity to 600 m/s when this occurs. Here, we choose Q_0 to be related to the shear-wave velocity by the relation $Q_{s0} = V_S 0.1$ and $Q_{p0} = 2Q_S$, in which V_S is in kilometers per second. We calculate Q_0 after imposing the lower limit on V_S; this ensures the minimum Q_0 is always > 20. We run two end-member models with $\gamma = 0.0$ and 0.8 (0.8 is the upper limit of the γ estimate of Song and Jordan, 2013, for southern California).

Figure 7 plots the modeled region, indicating the boundary and 110 strong ground motion stations from which data were obtained from the Center for Engineering Strong Motion Data database (see Data and Resources), to compare with our simulations. The simulation domain extends 56 km × 40 km in the east and north directions, respectively, to 24 km in depth, using a grid spacing of 8 m. We used Cerjan boundary conditions (sponge zone layers) in our 3D models, which dampens the reflections significantly, reducing energy that would reflect back into the model.

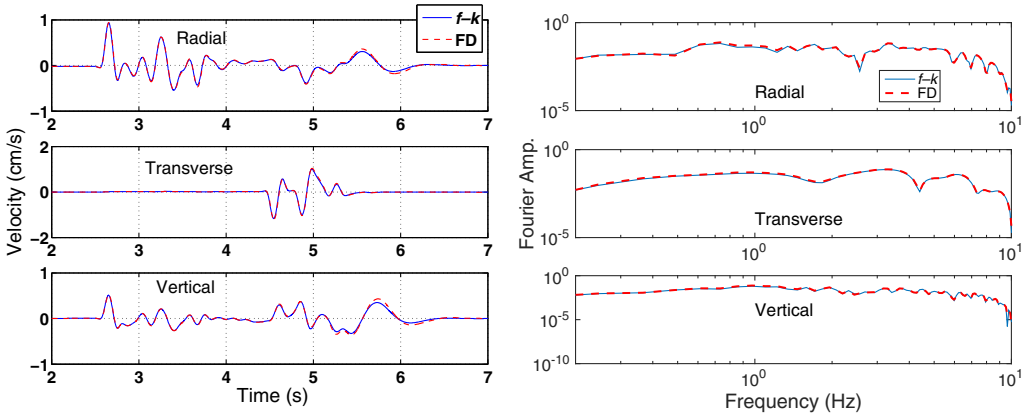

Figure 6. Layered-model point-source test: comparison of f-k and FD results for a $Q(f)$ model with $\gamma = 0.6$. The color version of this figure is available only in the electronic edition.

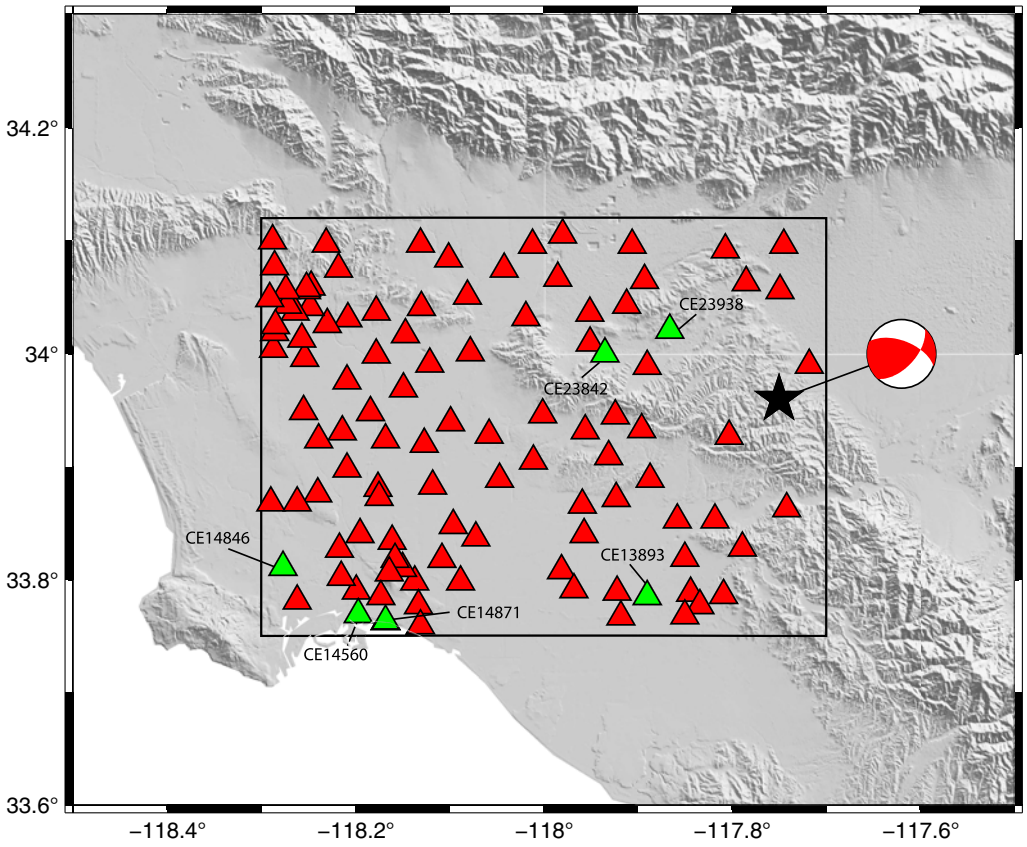

Figure 7. Simulated region of the Chino Hills event (rectangle) and locations of 110 strong ground motion stations (triangles) with the six named stations that are plotted in Figure 8. The star depicts the epicenter for the Chino Hills source. The color version of this figure is available only in the electronic edition.

In Figure 8, the east–west components of individual waveforms, as well as cumulative energy (integral of particle velocity squared) and Fourier amplitude spectra, are plotted at the stations highlighted in Figure 7, ordered with increasing distance to the fault.

The velocity waveforms were band-pass filtered between 0.1 and 4 Hz, while the energy plots are focused on the higher frequencies, calculated from seismograms band-pass filtered between 1.0 and 4.0 Hz. There are first-arrival amplitude differences between the two simulations and more energy in the coda for the $Q(f)$ model relative to the constant-Q model. The frequency domain shows the two simulations start to diverge above 1 Hz as expected, with $Q(f)$ having more energy. At stations near the source, the similarity between the synthetics and data in this frequency range is largely related to the accuracy of the source and site effects.

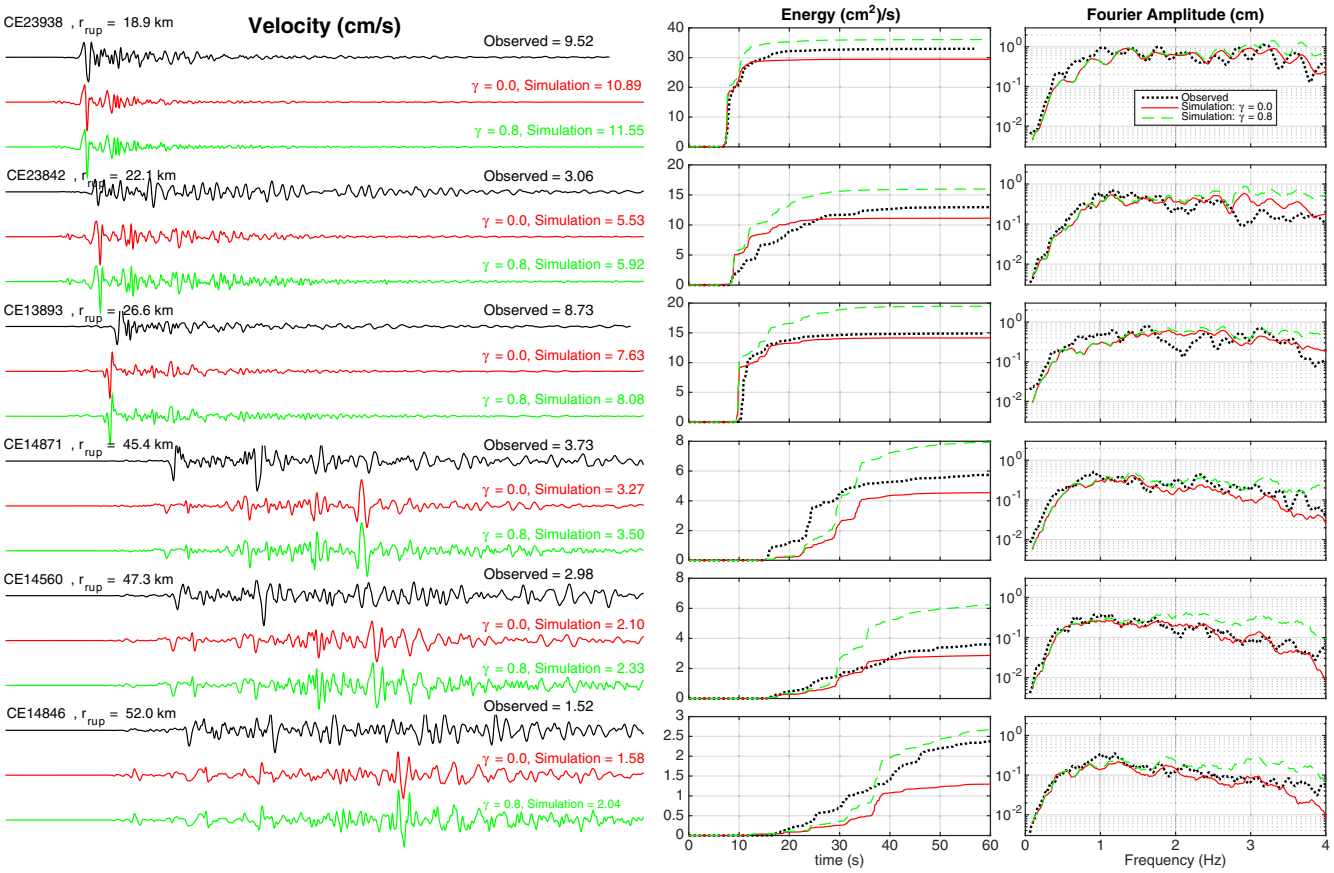

Figure 8. Comparison between data and synthetic velocity time-series, energy (normalized by density), and Fourier amplitude spectra for the east–west component of motion at stations ordered with increasing distance to the fault. The labels to the left show the station's network name and the distance to the epicenter, whereas the right labels show the peak ground velocity. The seismograms are bandpassed from 0.1 to 4 Hz, and the energy plots are bandpassed from 1.0 to 4.0 Hz. The color version of this figure is available only in the electronic edition.

At stations farther from the source, a greater difference between the two simulations is observed; it is clear that the $Q(f)$ model has significantly more energy. It is not evident whether constant Q or $Q(f)$ performs better compared with data when looking at individual stations.

To determine the significance of $Q(f)$ for the bulk of the data, we calculated the cumulative energy in the waveforms in the 1–4 Hz passband for each horizontal component and then computed the geometrical mean of these components for each station. Figure 9 plots the geometrical-mean cumulative energy as a function of the closest distance to the rupture plane R_{rup} for the strong ground motion stations in Figure 7. The differences between the data and constant-Q synthetics are similar to those between data and power-law Q synthetics at distances near the fault (<25 km). At further distances, however, there is a significant divergence between the constant-Q and power-law synthetics, with the power-law synthetics in better agreement with the data.

We next compare our $Q(f)$ simulations to several leading ground-motion prediction equations (GMPEs) (Boore and Atkinson, 2008; Campbell and Bozorgnia, 2008; Chiou and Youngs, 2008). These models are dependent on information about the source (M_{w}, width, etc.), as well as site effects (V_{S30} and others) and distance to the source R_{rup}. We compute orientation-independent median spectral motion (GMRotD50) (Boore *et al.*, 2006) at several periods for both the data and our synthetic models and compare these with the spectra predicted from the GMPEs. Figure 10 plots the range of the medians of the three different GMPE models at a period of 3 s. The five-point moving average of the observed data and the synthetic predictions is also plotted. We see the strong ground motion data are similar to those of the GMPE predictions but that there are significant differences between the data and synthetics. We attribute most of this misfit to inaccuracy in the source and the medium parameters (velocity and density), because stations near the source do not have a significant impact from Q. We see that both power-law simulations plot almost identically on top of one another, as they should at frequencies <1 Hz.

Figure 11 plots the same thing but at a period of 0.4 s. Here it is evident that the power-law model matches the decay in energy seen in the observations better than the constant-Q model, because less energy has been attenuated than by the constant-Q model. The effect becomes more important at distances farther from the source. Ⓔ Figure S2 plots the

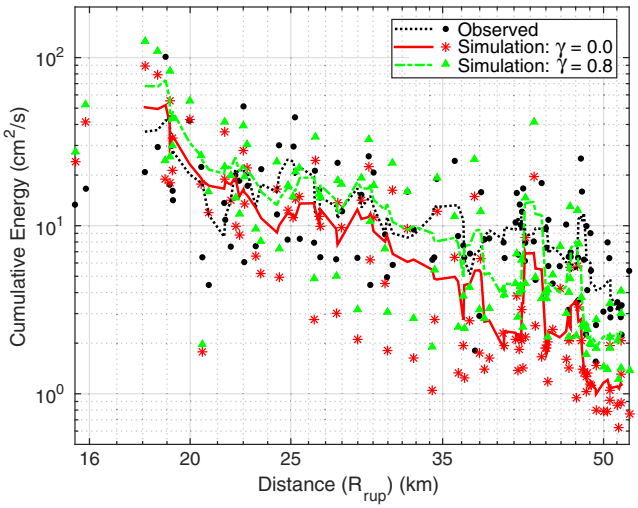

Figure 9. Cumulative energy as a function of distance to the fault for time series bandpassed between 1.0 and 4.0 Hz using the strong ground motion stations in Figure 7. The symbols depict values for individual stations, and lines depict a five-point moving average. R_{rup} indicates the closest distance to the ruptured surface of the fault plane. The color version of this figure is available only in the electronic edition.

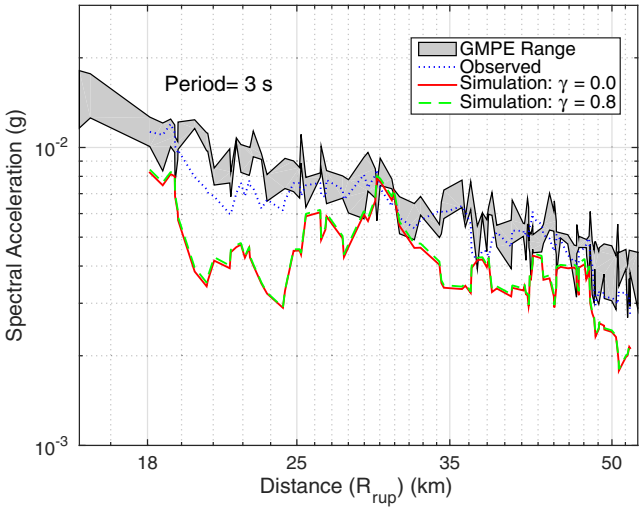

Figure 10. Median spectral acceleration as a function of distance centered at 3 s using the strong ground motion stations in Figure 7 compared with the range of several ground-motion prediction equation (GMPE) predictions. A five-point moving average was used for both synthetics and data for the strong ground motion station locations. R_{rup} indicates the closest distance to the ruptured surface of the fault plane. The color version of this figure is available only in the electronic edition.

comparison at a period of 1 s, showing differences of constant Q and $Q(f)$ intermediate between Figures 10 and 11.

The method of picking the peak spectral response includes information about a range of frequencies. Thus, we choose not to compute spectral accelerations above 2.5 Hz. Instead, we compute the Fourier spectral amplitude at several frequencies for both models and data by averaging the spectral

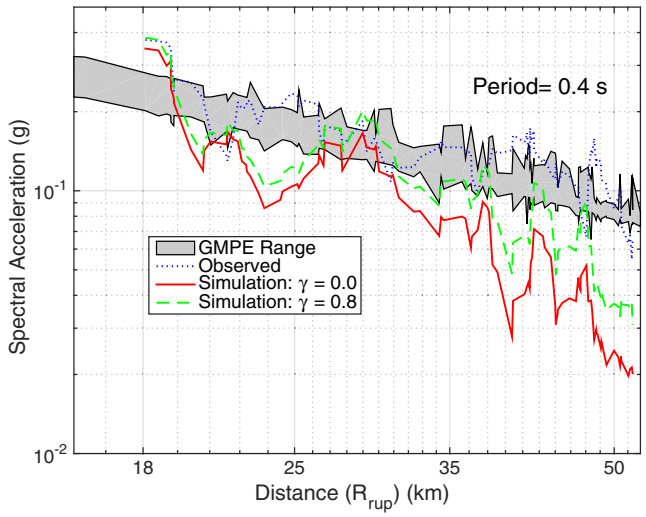

Figure 11. Similar to Figure 10 but at 0.4 s. The color version of this figure is available only in the electronic edition.

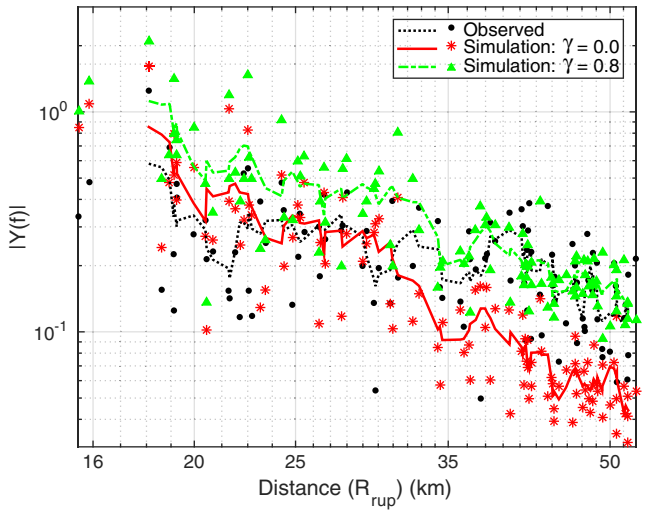

Figure 12. Fourier amplitude as a function of distance centered at 3.5 Hz using the strong ground motion stations in Figure 7. The symbols depict values for individual stations, and the lines depict a five-point moving average. R_{rup} indicates the closest distance to the ruptured surface of the fault plane. The color version of this figure is available only in the electronic edition.

amplitude in a narrow bandwidth (≈0.1 Hz) and plot those averages as a function of R_{rup}. Ⓔ Figures S3 and S4 show that we obtain qualitatively similar results to Figures 10 and 11 at frequencies of 0.25 and 2.5 Hz. Figure 12 shows the result at 3.5 Hz. Although the source model from Shao *et al.* (2012) was only constrained by seismic observations up to 2.5 Hz, the figure shows the model nonetheless generates 3.5 Hz spectral amplitudes that are consistent with observed spectra at station distances up to about 20 km, a distance range in which the Q model has a less appreciable effect. Thus, we use the source model without modification to examine the effect of the Q model on the 3.5 Hz amplitude decay at larger

distances. It is clear from Figure 12 that at distances larger than 25 km from the fault, constant-Q is too attenuating; whereas, although there is considerable scatter, the $Q(f)$ model with $\gamma = 0.8$ better matches the trend of observed amplitudes. The constant-Q model predicts amplitudes that are deficient by a factor of 3–5, relative to both the data and the $\gamma = 0.8$ power-law model, in the distance range considered.

These simulations used a velocity structure that is considered accurate only for estimating long-period ground motions. The waveforms would be expected to change significantly with the inclusion of scattering from small-scale heterogeneity in the media parameters. Current work is being performed to determine the significance and the role that scattering plays in ground-motion simulation (Savran and Olsen, 2014). The presence of additional scattering will add complexity to the wavefield and lengthen the coda, and scattering-model parameters may trade off with anelastic parameters. Preliminary calculations confirm, however, that those effects are unlikely to change our conclusion about the importance of including frequency-dependent Q in the model.

Discussion

Predicting amplitudes of high-frequency regional phases is important for discriminating explosions when events are small, as well as for accurate imaging in techniques determining the Earth's structure. Additionally, pushing deterministic simulations of earthquakes to higher frequencies is critically important for physics-based seismic-hazard analysis to enable structural engineers to design buildings and structures with shorter natural periods to withstand earthquake ground motions. Because recent work has improved the accuracy of the source at higher frequencies and as computational resources have become greater, realistic ground motion up to ≈10 Hz has become achievable at considerable distances from the source in a 3D medium. These synthetic ground motions have been shown to match the characteristics of real data, having a flat power spectrum up to some cutoff frequency (Shi and Day, 2013). However, the earthquake source is not the only source of complexity in the high-frequency ground motion; to model ground motions accurately, the medium needs to be realistically modeled as well. The model of anelastic attenuation is included within this complexity. As simulations extend to higher frequencies, energy losses from anelasticity become progressively more important because there are more wavelengths of propagation within a modeled domain.

Observations have shown that Q increases as frequency increases, changing from the constant behavior below 1 Hz or so. Here, we have implemented frequency-dependent Q into a staggered-grid velocity-stress FD code via a power-law function above a reference frequency f_T: $Q = Q_0 f^{\gamma}$, in which Q_0 and γ are constants that may vary with the region being studied (e.g., Phillips *et al.*, 2013). We used the low-loss approximation for $Q > 200$ and effective Q values lower than this.

The Q spectrum fits are generally accurate to within 5% across—two to three decades of bandwidth. We have seen that the scheme simulates broadband frequency-dependent Q accurately for both a half-space and a layered model, as verified by agreement with the respective analytical solutions. This includes both body waves, as well as surface waves. The lower limit of $Q = 15$ that we apply to our approach is not the lower bound; we choose a minimum Q value of 15, because this will be valid for almost all regions (except for very-low-velocity sediments) and allows us to accurately fit the rapidly changing coefficients at low values of Q with a simple interpolation formula. Additionally, for a given absorption bandwidth, the Q value has a lower bound determined by the thermodynamic constraint that the sum of the λ_k values be less than 1 (and the equivalent constraint in the coarse-grained approach is that each w_k value be less than 1).

The approach demonstrated here could be applied to other grid methods, both structured and unstructured, and extended using the coarse-grained technique as long as the coarse-graining periodicity is less than half the shortest seismic wavelength of interest (Day, 1998; van Driel and Nissen-Meyer, 2014). The same technique can be applied to solve for weights to fit a power law across all frequencies or a negative value of γ as found by Lindley and Archuleta (1992).

A benefit of this technique is its flexibility; the Q spectrum can be scaled to any value of $Q > 200$ by linear scaling of the weighting coefficients and transferred to the desired frequency range simply by dividing the set of relaxation times by the desired shifting factor. Additionally, only $3N$ coefficients (in which N is a small number, 8 in our examples) per Q model need to be tabulated, allowing for many different models to be easily stored in memory. In the future, as graphic processing unit hardware becomes less memory bound, it will likely become unnecessary to use the coarse-grained approximation, and thus a more simple interpolation procedure could be used to solve for the weighting coefficients in equation (7) down to very low values of Q, again using a linear-scaling relationship for large Q.

High-performance computing now allows seismologists to simulate the propagation of seismic waves through 3D complex crustal structures. This includes simulating the scattering effects caused by small-scale velocity and density heterogeneities in the medium that can affect the ground-motion intensity increasingly at higher frequencies. It is important to note that scattering from small-scale heterogeneities may play a large role in the effect of attenuation in the frequency range >1 Hz. It remains to determine the relative role of scattering versus intrinsic attenuation in high-frequency simulations and determine Q_{p0} and Q_{s0} in combination with scattering parameters. Additionally, the effects of nonplanar topography should be included in future studies, because this could also influence the scattering of energy.

Future work should explore regional variations in Q_0 and γ and examine the relationships of these parameters to seismic velocities, lithology, and tectonic setting. It remains to be determined whether the parameter κ in $\exp(-\pi\kappa f)$ pro-

posed by Anderson and Hough (1984), the high-frequency decay in Fourier amplitude spectra observed in ground-motion recordings, can be accurately modeled by some combination of depth variation and frequency dependence of Q. This parameter will become more important as ground-motion models are extended to frequencies beyond those covered here, in which the effects of κ are limited.

Conclusions

We developed an approach to determine the weighting coefficients in power-law Q models for use in time-domain wave-propagation techniques and found that we can fit low-order memory-variable approximations to those power laws to within 5% tolerance over two orders of magnitude in frequency. The resulting memory-variable models can be implemented either in conventional (point-wise) form or in a coarse-grained version. We verified the accuracy of the coarse-grained FD implementation by comparison of solutions with f-k synthetics for both uniform and layered-half-space models.

We illustrate the importance of including $Q(f)$ in ground-motion estimation by modeling the M_w 5.4 Chino Hills, California, earthquake. We find, by looking at both the distance decay of the Fourier amplitude spectrum and the cumulative energy of seismograms at various distances from the fault, that frequency-dependent Q does a better job than constant Q at frequencies above 1 Hz. $Q(f)$ is shown to become increasingly important at higher frequencies.

The utility of our approach will also extend to many other areas of seismology besides strong ground motion prediction, including explosion monitoring and seismic imaging, in which accurate prediction of amplitudes and arrival times are important.

Data and Resources

The seismograms from the 2008 M_w 5.4 Chino Hills earthquake used here were obtained from the archives of the Center for Engineering Strong Motion Data at http://www.strongmotioncenter.org/. The southern California velocity model v.4.26 can be obtained from Southern California Earthquake Center (SCEC) at http://scec.usc.edu/scecpedia/. Most of the data-processing work was done using MATLAB (http://www.mathworks.com/products/matlab/). Figures were prepared using MATLAB and the Generic Mapping Tools package (http://www.soest.hawaii.edu/gmt/). All websites were last accessed October 2014. All other data used in this article came from published sources listed in the references.

Acknowledgments

This research was supported by National Science Foundation (NSF) Award OCI-1148493 (SI2-SSI), through the Southern California Earthquake Center (SCEC), and by NSF Award EAR-1135455 (FESD). SCEC is funded by NSF Cooperative Agreement EAR-1033462 and U.S. Geological Survey (USGS) Cooperative Agreement G12AC20038. The Chino Hills simulations were generated on the Titan Cray XK7 at the Oak Ridge Leadership Computing Facility in Tennessee. Thanks to two anonymous reviewers for their help in improving the manuscript. This is SCEC publication number 6002

References

Anderson, J., and S. Hough (1984). A model for the shape of the Fourier amplitude spectrum of acceleration at high frequencies, *Bull. Seismol. Soc. Am.* **74,** 1969–1993.

Blanch, J., J. Robertsson, and W. Symes (1995). Modeling of a constant Q: Methodology and algorithm for an efficient and optimally inexpensive viscoelastic technique, *Geophysics* **60,** 176–184.

Boore, D. M., and G. M. Atkinson (2008). Ground-motion prediction equations for the average horizontal component of PGA, PGV, and 5%-damped PSA at spectral periods between 0.01 s and 10.0 s, *Earthq. Spectra* **24,** 99–138.

Boore, D. M., J. Watson-Lamprey, and N. A. Abrahamson (2006). Orientation-independent measures of ground motion, *Bull. Seismol. Soc. Am.* **96,** 1502–1511.

Campbell, K. W., and Y. Bozorgnia (2008). NGA ground motion model for the geometric mean horizontal component of PGA, PGV, PGD and 5% damped linear elastic response spectra for periods ranging from 0.01 to 10 s, *Earthq. Spectra* **24,** 139–171.

Chiou, B., and R. Youngs (2008). An NGA model for the average horizontal component of peak ground motion and response spectra, *Earthq. Spectra* **24,** 173–215.

Cui, Y., K. Olsen, T. Jordan, K. Lee, J. Zhou, P. Small, D. Roten, G. Ely, D. Panda, A. Chourasia, *et al.* (2010). Scalable earthquake simulation on petascale supercomputers, *Proc. of Supercomputing Conference*, New Orleans, Louisiana, 13–19 November.

Day, S. M. (1998). Efficient simulation of constant Q using coarse-grained memory variables, *Bull. Seismol. Soc. Am.* **88,** 1051–1062.

Day, S. M., and C. R. Bradley (2001). Memory-efficient simulation of anelastic wave propagation, *Bull. Seismol. Soc. Am.* **91,** 520–531.

Day, S. M., and J. B. Minster (1984). Numerical simulation of attenuated wavefields using a Pade approximant method, *Geophys. J. Roy. Astron. Soc.* **78,** 105–118.

Dunham, E. M., D. Belanger, L. Cong, and J. E. Kozdon (2011). Earthquake ruptures with strongly rate-weakening friction and off-fault plasticity, part 2: Nonplanar faults, *Bull. Seismol. Soc. Am.* **101,** 2308–2322, ISSN: 0037–1106.

Emmerich, H., and M. Korn (1987). Incorporation of attenuation into time-domain computations of seismic wave fields, *Geophysics* **52,** 1252–1264.

Erickson, D., D. McNamara, and H. Benz (2004). Frequency-dependent *Lg* Q within the continental United States, *Bull. Seismol. Soc. Am.* **94,** 1630–1643.

Fitchner, A., and M. van Driel (2014). Models and Frechet kernels for frequency-(in)dependent Q, *Geophys. J. Int.* **198,** 1878–1889.

Gottschämmer, E., and K. Olsen (2001). Accuracy of the explicit planar free-surface boundary condition implemented in a fourth-order staggered-grid velocity–stress finite-difference scheme, *Bull. Seismol. Soc. Am.* **91,** 617–623.

Graves, R. W., and B. T. Aagaard (2011). Testing long-period ground-motion simulations of scenario earthquakes using the M_w 7.2 El Mayor–Cucapah mainshock: Evaluation of finite-fault rupture characterization and 3D seismic velocity models, *Bull. Seismol. Soc. Am.* **101,** 895–907, ISSN: 0037–1106.

Graves, R. W., and S. M. Day (2003). Stability and accuracy analysis of coarse-grain viscoelastic simulations, *Bull. Seismol. Soc. Am.* **93,** 283–300.

Kohler, M., H. Magistrale, and R. Clayton (2003). Mantle heterogeneities and the SCEC reference three-dimensional seismic velocity model version 3, *Bull. Seismol. Soc. Am.* **93,** 757–774.

Komatitsch, D., Q. Liu, and J. Tromp (2004). Simulations of ground motion in the Los Angeles basin based upon the spectral-element method, *Bull. Seismol. Soc. Am.* **94,** 187–206.

Kristek, J., and P. Moczo (2003). Seismic-wave propagation in viscoelastic media with material discontinuities: A 3D fourth-order staggered-grid finite-difference modeling, *Bull. Seismol. Soc. Am.* **93,** 2273–2280.

Kristekova, M., J. Kristek, and P. Moczo (2009). Time-frequency misfit and goodness-of-fit criteria for quantitative comparison of time signals, *Geophys. J. Int.* **178,** 813–825.

Lee, E., and P. Chen (2014). Full-3-D tomography for crustal structure in southern California based on the scattering-integral and the adjoint-wavefield methods, *J. Geophys. Res.* **119,** 1–31.

Lekic, V., J. Matas, M. Panning, and B. Romanowicz (2009). Measurement and implications of frequency dependence of attenuation, *Earth Planet. Sci. Lett.* **282,** 285–293.

Lindley, G., and R. Archuleta (1992). Earthquake source parameters and the frequency dependence of attenuation at Coalinga, Mammoth Lakes, and the Santa Cruz Mountains, California, *J. Geophys.* **97,** 14,137–14,154.

Liu, H., D. Anderson, and H. Kanamori (1976). Velocity dispersion due to anelasticity; implications for seismology and mantle composition, *Geophys. J. Int.* **47,** 41–58.

Liu, P., and R. Archuleta (2006). Efficient modeling of Q for 3D numerical simulation of wave propagation, *Bull. Seismol. Soc. Am.* **96,** 1352–1358, ISSN: 0037–1106.

Ma, S., and P. Liu (2006). Modeling of the perfectly matched layer absorbing boundaries and intrinsic attenuation in explicit finite-element methods, *Bull. Seismol. Soc. Am.* **96,** 1779–1794.

Magistrale, H., S. Day, R. Clayton, and R. Graves (2000). The SCEC southern California reference three-dimensional seismic velocity model version 2, *Bull. Seismol. Soc. Am.* **90,** no. 6B, S65–S76.

McNamara, D., M. Meremonte, J. Z. Maharrey, S.-L. Mildore, J. R. Altidore, D. Anglade, S. E. Hough, D. Given, H. Benz, L. Gee, *et al.* (2012). Frequency-dependent seismic attenuation within the Hispaniola Island region of the Caribbean Sea, *Bull. Seismol. Soc. Am.* **102,** 773–782, ISSN: 0037–1106.

Moczo, P. (2005). On the rheological models used for time-domain methods of seismic wave propagation, *Geophys. Res. Lett.* **32,** 1–5, ISSN: 0094–8276.

Olsen, K., R. Nigbor, and T. Konno (2000). 3D viscoelastic wave propagation in the Upper Borrego Valley, California, constrained by borehole and surface data, *Bull. Seismol. Soc. Am.* **90,** 134–150.

Phillips, W. S., K. M. Mayeda, and L. Malagnini (2013). How to invert multi-band, regional phase amplitudes for 2-D attenuation and source parameters: Tests using the USArray, *Pure Appl. Geophys.* **171,** 469–484.

Raoof, M., R. Herrmann, and L. Malagnini (1999). Attenuation and excitation of three-component ground motion in southern California, *Bull. Seismol. Soc. Am.* **89,** 888–902.

Savage, B., D. Komatitsch, and J. Tromp (2010). Effects of 3D attenuation on seismic wave amplitude and phase measurements, *Bull. Seismol. Soc. Am.* **100,** 1241–1251, ISSN: 0037–1106.

Savran, W. H., and K. B. Olsen (2014). Validation exercise for two southern California earthquakes, *Procs. 2014 SCEC Annual Meeting*, Palm Springs, California, 7–10 September 2014, Poster Number 65.

Shao, G., C. Ji, and E. Hauksson (2012). Rupture process and energy budget of the 29 July 2008 M_w 5.4 Chino Hills, California, earthquake, *J. Geophys.* **117,** 1–12.

Shi, Z., and S. M. Day (2013). Rupture dynamics and ground motion from 3-D rough-fault simulations, *J. Geophys.* **118,** 1122–1141, ISSN: 21699313.

Song, X., and T. H. Jordan (2013). Anelastic attenuation and elastic scattering of seismic waves in the Los Angeles region, *American Geophysical Union Annual Meeting*, San Francisco, California, 9–13 December 2013, Poster Number S32B-05.

Taborda, R., and J. Bielak (2014). Ground-motion simulation and validation of the 2008 Chino Hills, California, earthquake using different velocity models, *Bull. Seismol. Soc. Am.* **104,** 1876–1898.

Tape, C., Q. Liu, A. Maggi, and J. Tromp (2010). Seismic tomography of the southern California crust based on spectral-element and adjoint methods, *Geophys. J. Int.* **180,** 433–462.

van Driel, M., and T. Nissen-Meyer (2014). Optimized viscoelastic wave propagation for weakly dissipative media, *Geophys. J. Int.* **199,** 1078–1093.

Xie, X.-B. (2005). Investigating explosion source energy partitioning and Lg-wave excitation using a finite-difference plus slowness analysis method, *Bull. Seismol. Soc. Am.* **95,** 2412–2427.

Xu, T., and G. McMechan (1998). Efficient 3-D viscoelastic modeling with application to near-surface land seismic data, *Geophysics* **63,** 601–612.

Zhu, L., and L. Rivera (2002). A note on the dynamic and static displacements from a point source in multilayered media, *Geophys. J. Int.* **148,** 619–627.

San Diego State University
Department of Geological Science
5500 Campanile Drive
San Diego, California 92182
withers@rohan.sdsu.edu
kbolsen@mail.sdsu.edu
sday@mail.sdsu.edu

Manuscript received 10 September 2015;
Published Online 03 November 2015